ACS APPLIED MATERIALS & INTERFACES

RESEARCH ARTICLE

www.acsami.org

All Solution-Processed, Fully Transparent Resistive Memory Devices

Areum Kim,[†] Keunkyu Song,[†,‡] Youngwoo Kim,[†] and Jooho Moon*[,†]

[†]Department of Materials Science and Engineering, Yonsei University, 134 Shinchon-dong Seodaemun-gu, Seoul, 120-749, Korea

[‡]LCD R&D Center, Samsung Electronics Co. LTD., Gyeonggi-do 449-711, Korea

Supporting Information

ABSTRACT: We fabricated all-solution processed, fully transparent resistive random access memory (*sol*-TRRAM) with a configuration of ITO/GaZnO(GZO)/ITO. All layers, including an active layer and top and bottom ITO electrodes, were deposited on a glass substrate by either spin coating or inkjet printing using a sol−gel solution. Our *sol*-TRRAM was transparent, with 86.5% transmittance at 550 nm. An initial forming process is unnecessary for the production of transparent memory due to the presence of sufficient inherent nonlattice oxygen ions in the solution-processed GZO layer. The *sol*-TRRAM also showed reasonable bipolar resistance switching with a low operation current (<100 μA) and excellent cycle endurance properties (>300 cycles). The main conduction mechanism during the set process can be explained by the trap-controlled space-charge limited conduction, and the resistance change occurred by the modification of the potential barrier height because of the charge injection by Fowler−Nordheim tunneling.

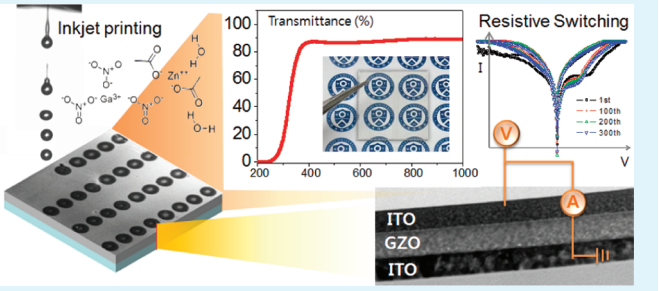

KEYWORDS: transparent electronics, transparent memory device, solution processing, indium tin oxide, resistive random access memory, zinc oxide

1. INTRODUCTION

Transparent electronics is one of the most important emerging technologies for next generation electronic systems,[1,2] and has recently attracted great interest due to its potential to make significant impacts in fields like transparent displays, transparent energy storage, ultraviolet (UV) detectors, and solar cells.[1−4] Transparent wide-band gap materials with well-controlled carrier concentrations are necessary for the development of transparent electronics such as degenerately doped oxides ($\sim 1 \times 10^{21}$ cm^{-3}) referred to as transparent conductive oxides (TCO) that include indium tin oxide (ITO) and Al-doped ZnO. Alternatively, oxides with intermediate carrier concentrations (1×10^{14} to 1×10^{18} cm^{-3}) can be utilized in field-effect transistors as an active channel.[5] Fully transparent field-effect transistors based on ZnO and related oxides have been actively investigated, and transparent nonvolatile memory devices based on the oxide semiconductor TFT have been also demonstrated, but they suffer from high voltage operation, complicates structure, and short retention time.[6,7]

Resistive random access memory (RRAM) is promising due to characteristics such as nonvolatility, low power consumption, fast operation speed, and simple structure, and can serve as a substitute for flash memory, which is hampered by scaling-down limitations. Resistive switching phenomena have been observed in various oxides, such as TiO_2,[8,9] NiO,[10] ZnO,[11,12] HfO_2,[13,14] Ta_2O_3,[15] WO_3,[16] and MnO_2.[17] These oxides are mostly transparent, with wide-band gap energies, and therefore RRAM is a good candidate for enabling transparent memory. After the first demonstration of fully transparent RRAM (TRRAM) in a structure of ITO/ZnO/ITO by Seo et al.,[18] configurations such as ITO/TiO_2/ITO,[19] ITO/Mg:ZnO/FTO,[20] ITO/Gd_2O_3/ITO,[21] ITO/InGaZnO/ITO,[22] Al:ZnO/Mg:ZnO/Al:ZnO,[11] and Ga:ZnO/ZnO/Ga:ZnO[23] have been reported. The active layers are either vacuum-deposited or solution-processed, whereas the transparent electrodes are usually deposited by radio frequency (rf) magnetron sputtering. This vacuum processing increases manufacturing costs, which is problematic for applications in modern, mass-produced electronics. Scalable large-area manufacturing based on solution processing is of growing interest, with the ultimate goal of fabricating invisible electronics. It should be noted that solution-processed Ag nanowire/TiO_2/Ag nanowire RRAM has only been recently developed,[24] but the transmittance of the polyethylene terephthalate(PET)/Ag nanowire/TiO_2 is only 66.5% at 550 nm and the device is nearly opaque.

In this paper, we fabricated all solution-processed, fully transparent RRAM (*sol*-TRRAM) using a ITO/GaZnO(GZO)/ITO configuration. All layers, including the active layer and top and bottom ITO electrodes, were fabricated by solution processing with spin coating and inkjet printing. The *sol*-TRRAM shows high transmittance in the visible band and reasonable resistance switching behavior.

2. RESULTS AND DISCUSSION

Figure 1 shows our *sol*-TRRAM devices in a configuration of ITO/GZO/ITO on glass substrates. The devices were truly

Received: September 8, 2011
Accepted: October 20, 2011
Published: October 20, 2011

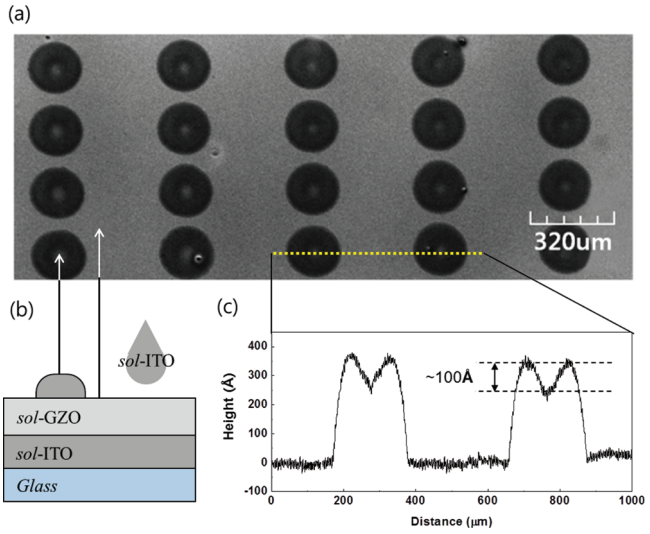

Figure 1. (a) UV-laser confocal image of inkjet printed ITO electrodes on a GZO/spin-coated ITO/glass substrate. (b) Schematic of an all-solution processed ITO/GZO/ITO RRAM device. (c) Surface profile of the top electrodes following the yellow line in (a).

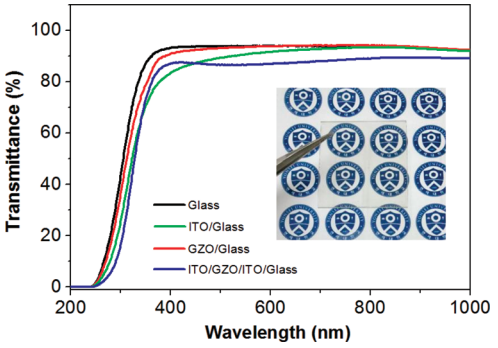

Figure 2. UV−vis transmittance of bare glass (black), ITO/glass (green), GZO/glass (red), ITO/GZO/ITO/glass (blue). To determine the optical properties, both the ITO bottom and top layers were spin-coated four times, resulting in a film with a thickness of ∼30 nm. The inset is a photograph of the *sol*-TRRAM (ITO/GZO/ITO/glass) device. The background is observed through the device without refraction or distortion.

transparent in the visible band, as shown in Figure 2 (inset), such that their features were detectable by confocal laser scanning microscopy as shown in Figure 1a. Inkjet printing of the ITO ink resulted in a dot-shaped top electrode array with spacing of 200 μm in the *x*-direction and 500 μm in the *y*-direction. The line profile of the ITO top electrodes is shown in Figure 1c. Thickness differences between the edge and center can be attributed to a coffee-ring effect during the drying of inkjet printed ITO ink.[25] The peak-to-valley height ratio of an electrode was ∼100 nm and the diameter of the top electrode was ∼200 μm. To quantitatively evaluate the transparency, we measured the transmittance of ITO/glass and GZO/glass, which were 90.6 and 93.5% at 550 nm, respectively (Figure 2). The solution-processed ITO and the solution-processed GZO are good candidates for use as transparent materials in RRAM. The sandwich structure of ITO/GZO/ITO was still highly transparent with a transmittance of 86.5% at 550 nm, which is very transparent compared to

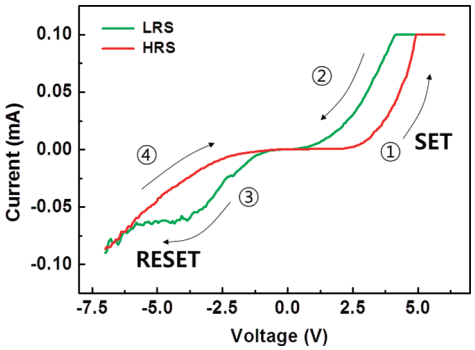

Figure 3. Bipolar resistance switching curves for the all-solution processed ITO/GZO/ITO RRAM. DC voltage was applied to the top ITO electrode in a sequence of 0 → 6 → 0→ −7 → 0 V with a compliance current 100 μA. SET occurred in the positive region and then the high resistance state (HRS) changed to a low resistance state (LRS). In the negative voltage region, RESET occurred and LRS changed to HRS.

solution-processed RRAM using Ag nanowire/TiO_2/Ag nanowire (transmittance of 66.5% at 550 nm). These high transmittance properties indicate that our ITO/GZO/ITO is a suitable configuration for use in fully transparent memory devices.

Figure 3 shows the bipolar *I*−*V* switching characteristics of *sol*-TRRAM under the applied DC voltage bias at room temperature. DC voltage was applied to the top ITO electrode in a sequence of 0 → 6 → 0→ −7 → 0 V. Compliance currents were fixed at 100 μA in both the positive and negative voltage regions to prevent permanent breakdown of the devices. The SET occurred in the positive voltage region and the RESET was observed in the negative voltage region. Despite the device involved, the relatively large electrode (∼200 μm) used, and the possibility that the solution-processed active layer may contain defects, the RESET current of our *sol*-TRRAM was less than 100 μA with self-compliance. This current level was less than values reported for other ZnO based RRAMs (1×10^{-3} to 1×10^{-1}A).[11,12,23,26] The low RESET current is an important factor in RRAM operation, because it enables low power consumption. Our *sol*-TRRAM was operated in a higher voltage region of −7 to +6 V compared to other RRAM devices using ITO electrodes. We believe that this discrepancy is related to the relatively high resistivity associated with solution-deposited ITO compared to sputtered ITO (see the Supporting Information, Figure S1). To investigate the endurance property of *sol*-TRRAM, we performed continuous voltage scans on devices over 350 switching cycles with a current compliance of 100 μA at room temperature. The resistances of each LRS and HRS measured at 0.3 V were nearly constant with no device damage or breakdown during cycles. The on/off ratio was displayed at approximately 15, as illustrated in Figure 4a. The resistance fluctuations at both the on and off states must be small during endurance tests to indicate reliable memory devices. Our device demonstrated stable resistance states up to 350 cycles. Figure 4b shows the *I*−*V* switching curve of *sol*-TRRAM in the semilogarithmic plot. The *I*−*V* curves of the first, 100th, 200th, and 300th sweep are selected to reveal a degree of the *I*−*V* characteristic variations during the repeated cycles. Although the initial *I*−*V* curve exhibited a slightly higher SET voltage and lower RESET current level, the *I*−*V* curves of the 100th, 200th, and 300th sweeps nearly overlapped.

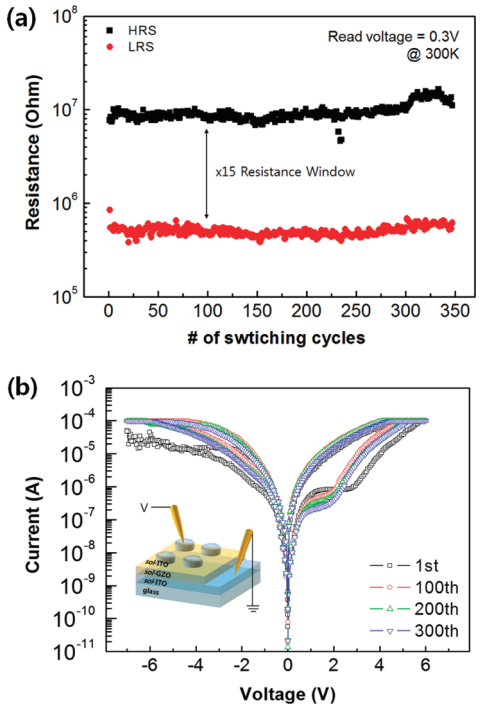

Figure 4. (a) Cycle endurance of *sol*-TRRAM at room temperature. The read voltage was 0.3 V and the on/off ratio was approximately 15. (b) *I*−*V* switching curve of *sol*-TRRAM in a semilogarithmic plot. The 1st, 100th, 200th, and 300th *I*−*V* curves are extracted during the total 350 sweep cycles.

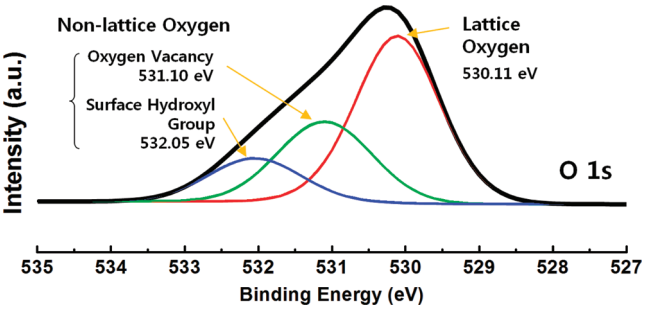

Figure 5. X-ray photoelectron spectroscopy data for the as-fabricated GZO thin film layer. In the O 1s core level spectra, the lattice peak (530.11 eV) and additional peaks (531.10, 532.05 eV) were observed.

Our *sol*-TRRAM device was operated without an additional forming process to initiate resistance switching. The forming process is a one-time application of high voltage or current that produces significant change in electronic conductivity.[28−31] After forming, devices operate as tunable resistance switches, but with a wide variance of electrical properties depending on the details of the forming process.[32] Thus, the forming step can limit the device design and practical applications of RRAM. Although several binary oxides with appropriate oxidation, such as CuO and NiO, do not require forming processes, all of these devices suffer from unstable resistance switching or insufficient endurance.[33] The stable bipolar resistance switching of our *sol*-TRRAM without a forming process is attributed to the as-fabricated GZO layer, which retains sufficient nonlattice oxygen ions such as oxygen vacancies that are responsible for resistance

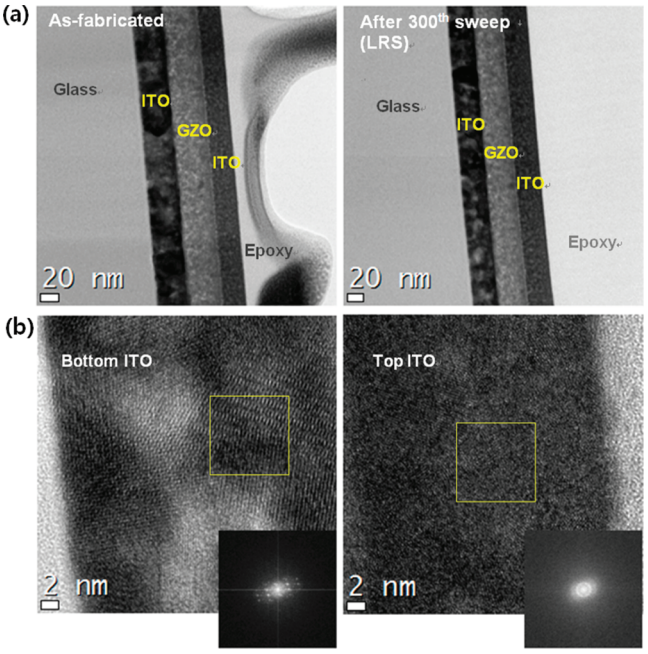

Figure 6. (a) HR-TEM cross-sectional images of *sol*-TRRAM (ITO/GZO/ITO). The left image is the as-fabricated device and the right image is the SET device after more than 350 cycles. (b) Cross-sectional images of bottom ITO electrode (left) and top ITO electrode (right) for the as-fabricated device. The bottom ITO was polycrystalline and the top ITO was amorphous. The inset represents a Fast Fourier transform image obtained from the marked region of HR-TEM.

change.[22] We believe that the GZO thin film annealed at 500 °C is mainly amorphous, with some nanocrystallites of zinc gallate or ZnO (see the Supporting Information, Figure S2). The presence of nonlattice oxygen ions in the film can be supported by X-ray photoelectron spectroscopy (XPS) analysis of the GZO thin film, as shown in Figure 5. The XPS peaks for the O1s core level may be consistently fitted by three different near-Gaussian subpeaks, centered at 530.11, 531.10, and 532.05 eV. The dominant peak located at 530.11 eV was assigned to O^{2-} ions from oxide lattices, while the peaks located at 531.10 and 532.4 eV were associated with nonlattice oxygen ions, such as oxygen vacancies and surface hydroxyl groups.[35,36] Based on these XPS results, the GZO thin film contains significant numbers of nonlattice oxygen ions. The presence of nonlattice oxygen ions likely plays an important role in the resistive change and requires further investigation. Sufficient nonlattice oxygen ions in the GZO thin film allows our *sol*-TRRAM to be operated without a forming process.

Microstructural evidence can provide a clear understanding of the on/off operating mechanism associated with RRAM. In previous studies, high resolution transmission electron microscopy (HR-TEM) analysis revealed that Magnéli nanofilaments connecting top and bottom electrodes were observed in the SET sample, while the nanofilaments were disconnected in the RESET sample.[8] Alternatively, Jeong et al.[37] observed that the variation of oxygen ions accumulated or were released by oxidation−reduction at the TiO_2 and Al interface during on/off switching in the Al/TiO_2/Al system. Similarly, we prepared two samples with different resistance states to monitor microstructural changes in the *sol*-TRRAM. Figure 6a shows a HR-TEM cross-sectional image of the as-fabricated sample (6a left) under an initial high resistance state (HRS), and a sample

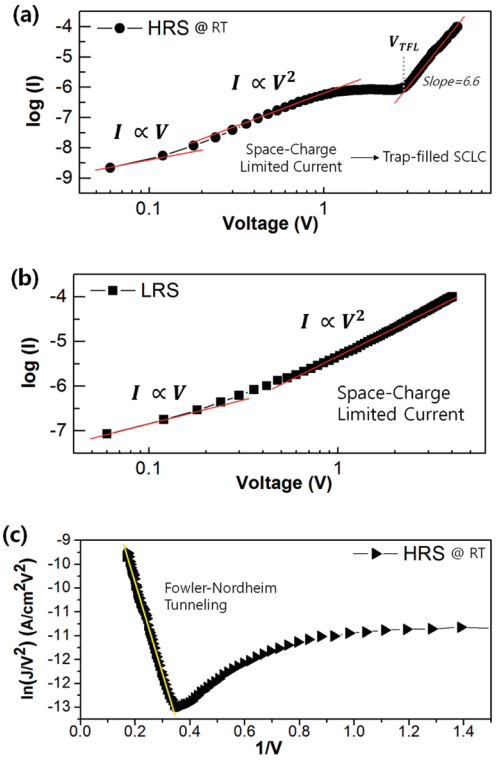

Figure 7. To analyze the SET mechanism, we replotted the $I-V$ curves measured at room temperature in the positive voltage region (①,② sections in Figure 3). In the high resistance state (HRS), (a) space-charge-limited conduction (SCLC) → trap-filled SCLC. (b) SCLC in the low resistance state (LRS). (c) The linear relationship and the negative slope of the HRS current in the $\log(J/V^2) - \log(1/V)$ plot indicate the Fowler−Nordheim current transport above the V_{TFL} region.

operated for 300 sweep cycles and then SET to the low resistance state (LRS) (6a right). There was no noticeable microstructural variation between the as-fabricated device and the device when they were cycled 350 times. Neither a filament-like structure in the GZO film nor an additional interfacial layer at the ITO-GZO interface were observed. Microstructural analysis indicated that the resistive switching in our *sol*-TRRAM occurs without significant structural changes. This invariance is advantageous for stable device operation as shown in Figure 4. Repeated significant structural changes during the operation impose physical loads on devices, and switching stability and device life are adversely affected. Figure 6b shows magnified cross-sectional images of the bottom ITO electrode (left) and top ITO electrode (right) of the as-fabricated device. The bottom ITO layer contained crystal domains, while no crystallites were observed in the top ITO layer. Fast Fourier transform (FFT) obtained from HR-TEM images (inset) also revealed differences in the phases between the top and bottom ITO electrodes. Although both the top and bottom ITO electrodes were deposited from the same sol−gel solution, each layer underwent a different fabrication method and heat treatment history. The top electrode was deposited by inkjet printing and annealed once at 500 °C, whereas the spin-coated bottom electrode received three consecutive annealing treatments (after deposition, during GZO deposition, and during top ITO deposition). As a result, the inkjet printed top ITO electrode was amorphous, while the spin-coated bottom ITO electrode had sufficient time to be converted into a polycrystalline film during multiple annealing steps. The different amounts of crystallinity of the bottom and top ITO electrodes likely lead to different conductivities. In addition, the bottom ITO layer was exposed to an O_2 plasma treatment to form a hydrophilic surface for better film deposition of the subsequent GZO layer. O_2 plasma treatment may alter the work function of the ITO film.[38] These differences in the work function and conductivity between the top and bottom electrodes can modify the Schottky barrier height at each interface, resulting in asymmetric $I-V$ switching curves shown in Figure 4b.[39] To support the existence of Schottky barrier at bottom electrode and the asymmetric work function of top and bottom electrode, the $I-V$ measurements were performed by changing the directions of ground and DC bias application (see the Supporting Information, Figures S3−S6.)

The $I-V$ characteristics measured in Figure 3 were replotted to clarify the SET mechanism in the *sol*-TRRAM. The conduction modes can be distinguished via isothermal $I-V$ correlation.[40] For example, $I \propto V$ for ohmic conduction, $\ln I/V \propto V^{0.5}$ for Poole-Frenkel emission, and $\ln I/V^2 \propto V^{-1}$ for Fowler-Nordheim (FN) tunneling with T as the absolute temperature. Figure 7a and 7b show the logarithmic plots of the $I-V$ curves for the positive voltage sweep region. Figure 7a indicates the HRS, and the initial section of the $I-V$ curve showed linear behavior with a $I \propto V$ relationship (slope ~1). This relationship indicates that ohmic conduction is a key conduction mechanism in this range. Ohmic conduction results from the fact that the injected carrier density is less than the thermally generated carrier density. In the high-voltage region where $V > 0.2$ V, space-charge limited conduction (SCLC) becomes dominant in the GZO thin film. In the defect-free crystal, SCLC can be described by Mott's V^2 law[41]

$$J = 9\varepsilon_0\varepsilon_r\mu_p V^2/8d^3$$

where μ_p is the hole mobility, V is the applied voltage, d is the thickness, ε_o is the permittivity of free space, and ε_r is the static dielectric constant. However, as demonstrated in the XPS results, the GZO film contains considerable defects, such as nonlattice oxygen ions. Defects in the GZO film could form trap sites below the conduction band, where the injected charge carriers can be entrapped. Thus, the SCLC model should be modified according to the concept of shallow traps.[42] Since shallow traps below the conduction band entrap the injected charge carriers, the density of the injected charge carriers that freely contribute to the SCLC is reduced by the factor θ, and the ratio of the total density of free electrons n_f to the trapped electrons n_t is given by:

$$\theta = \frac{p}{(p + p_t)}$$

where p is the density of free carriers and p_t is the density of trapped carriers. When all the available traps are filled by the applied voltage, the current density abruptly increases with a $I-V$ slope greater than 2 and the voltage where the current density increases is called the trap-filled limit (TFL), V_{TFL}. This phenomenon was also observed in our device, as shown in Figure 7a, where the current abruptly increased at a voltage greater than V_{TFL} and its slope reached 6−7. In the same voltage region (i.e., greater than V_{TFL}), the $I-V$ correlation was well fit to the $\ln(J/V^2) - 1/V$ plot with a negative slope, as shown in Figure 7c, indicating Fowler−Nordheim (FN) tunneling.[43] FN tunneling is a conduction mechanism in thin dielectric films under high

electric field, where the charge carriers are injected from the electrode to the insulator by tunneling through a potential barrier. This analysis suggests that the mechanism of the SET process is due to the FN tunneling when the voltage reaches the trap-filled limited region above V_{TFL}. The possible SET mechanism from these results is that the accumulation of injected charge carriers at the interface between ITO and GZO layers by FN tunneling could modify the potential barrier height, which alters the resistance state from HRS to LRS. The $I-V$ graph in the LRS region was also fitted in a log I − log V plot, as shown in Figure 7b. In the high-voltage region, the log I − log V slope was approximately 2, indicating that the dominant conduction mechanism of LRS is the SCLC model with no traps. The conduction in the low-voltage region can be expressed by the ohmic conduction. With respect to the logarithmic plot of the $I-V$ curve in the HRS (Figure 7a), the log I − log V plot in the LRS was a better linear fit, suggesting that the trapped carriers are not released completely with reduced voltage.[44] The HRS and LRS states in our *sol*-TRRAM can be well-described by the SCLC model in which shallow traps reduce the HRS current and the LRS current approaches the trap-filled SCLC as the traps get filled by the applied bias.

During the RESET process, there was gradual change in the resistance state (Figure 4b) instead of an abrupt current transition. Kinoshita et al.[45] observed a similar phenomenon in Ga-doped ZnO RRAM, suggesting that Ga-doping is responsible for the gradual resistance change observed during the RESET process. In pure ZnO, the dominant carriers are injected by oxygen vacancies. When the reset voltage is applied, the recovery between oxygen vacancies and movable oxygen occurs by Joule heating.[46] Therefore, the current flow in the ZnO film will decrease rapidly because of a drastic decrease in the carrier density, because nearly all the carriers in ZnO are injected by the oxygen vacancies. However, in the case of GZO, Ga^{3+} introduction into the ZnO matrix can introduce donor defects by Ga^{3+} substitution of Zn^{2+}, increasing the charge carrier concentration.[47] Then, the carriers induced by Ga substitution remain in the GZO film, even if the carriers injected by the oxygen vacancies diminish. Thus, doped Ga generates residual carriers that hinder rapid cooling, even after the drastic decrease in carriers injected by the oxygen vacancies during the RESET process.

3. CONCLUSIONS

We fabricated all-solution processed, fully transparent resistive memory devices. All layers, including the GZO layer and top and bottom ITO electrodes, were deposited by spin coating and inkjet printing using sol−gel solutions to implement a sandwiched structure with a ITO/GaZnO(GZO)/ITO configuration. Our *sol*-TRRAM was truly transparent, with a transmittance of 86.5% at 550 nm. The *sol*-TRRAM also showed reasonable bipolar resistance switching behavior with a low operation current (<100 μA) and excellent cycle endurance (>300 cycles). Our transparent memory devices do not require an initial forming process. XPS analysis revealed that considerable amounts of nonlattice oxygen ions exist in the GZO film, and these nonlattice oxygen ions allow the forming operation to be omitted. The SET mechanism was investigated by isothermal $I-V$ curve fitting. The main conduction mechanism during the SET process can be explained by the SCLC model, in which the SET occurred through the modification of potential barrier height due to charge injection by FN tunneling. HR-TEM analysis confirmed that our *sol*-TRRAM involves the electrical resistive change mechanism without the formation of a structural filament or additional interfacial layer. This resistive switching behavior, which occurs without significant microstructural changes, is advantageous for use in memory devices with stable switching and long lifetimes. Asymmetric $I-V$ switching phenomena resulted from the difference in physical characteristics between the top and bottom ITO electrodes, which received different heat- and surface-treatments. Gradual resistance transition behavior observed during the RESET process can be explained by the Ga doping effect. With excellent transparent properties and reasonable resistance switching behavior, *sol*-TRRAM is promising for use in future RRAM applications. Furthermore, our all-solution processed transparent memory devices could pave the way for transparent electronics and other future applications, including flexible electronic papers and smart window.

4. EXPERIMENTAL SECTION

Preparation of ITO Films. The sol−gel solution used for ITO electrodes was prepared by dissolving indium nitrate hydrate ($In(NO_3)_3 \cdot H_2O$, Aldrich), and tin(IV) acetate ($Sn(CH_3COO)_4$, Aldrich) in 2-methoxyethanol (anhydrous, 99.8%, Aldrich).[48] The total concentration of metal precursors was 0.2 *M* and the molar ratio of In: Sn was 95: 5. Ethanolamine (≥99.0%, Aldrich) was used as a stabilizing agent to improve the solubility of the precursor salts and formamide (≥99.5%, Aldrich) was used to enhance coating properties. The ITO bottom electrode layer was deposited on the glass substrate by spin coating at 3000 rpm for 30s. The glass substrate was cleaned with isopropyl alcohol and O_2 plasma cleaner prior to deposition. Four coatings were performed to obtain sufficient thickness with low sheet resistance. The resulting films were annealed at 500 °C for 2 h. Both ITO and GZO sol−gel solutions were filtered with a 0.2 μm membrane (poly(tetrafluoroethylene), Whatman) prior to spin-coating and inkjet printing.

Preparation of GZO Films. For the active layer, we synthesized a gallium zinc oxide (GZO) sol−gel solution at 0.4 M. Gallium nitrate hydrate ($Ga(NO_3)_3 \cdot xH_2O$, Aldrich) and zinc acetate dihydrate ($Zn(CH_3COO)_2 \cdot 2H_2O$, 99.999%, Aldrich) are dissolved in 2-methoxyethanol and the molar ratio of Ga:Zn was 1:1. Ethanolamine was used as a stabilizing agent. The GZO layer was obtained by spin coating, followed by annealing at 500 °C for 4 h.

Inkjet Printing of Top ITO Electrodes. After the annealing of the GZO active layer, top contact electrode deposition was performed by inkjet printing using the same ITO solution as the spin coating. The printer setup consisted of a drop-on-demand (DOD) piezoelectric inkjet nozzle with an orifice size of 50 μm (MicroFab Technologies, Inc., Plano, TX, USA). The gap between the surface and nozzle was approximately 0.5 mm during printing. Uniform droplet ejection was achieved by applying 4 μs long, 40 V pulses at a frequency of 1000 Hz. Inkjet printed ITO top electrodes annealed at 500 °C for 2 h had a circular shape with a diameter of ∼200 μm.

Characterization. The cross sectional morphology of the inkjet printed ITO top electrodes was characterized by a surface profiler (Dektak 150, Veeco). Each layer thickness for the ITO(*bottom*)/GZO/ITO(*top*) was ∼33 nm, 30 nm, and 34 nm, respectively, as determined by high resolution transmission electron microscopy (HR-TEM, Titan, FEI). Current−voltage ($I-V$) characteristics were measured by an Agilent B1500 parameter analyzer. During the measurements, a DC voltage bias was applied to the top electrode while the bottom electrode was grounded. All the measurements were performed

at room temperature in the dark. Sheet resistances of the solution-deposited ITO electrodes were determined by four-point probe measurement (Model RG-100, Napson Corp.). The phase identification, microstructure, and surface chemical structure of the films were analyzed using high resolution X-ray diffraction (X PET-PRO MRD, Phillips), HR-TEM, and XPS. The optical properties of the spin-coated multilayered ITO/GZO/ITO films on glass were measured by a UV−vis spectrophotometer (V530, JASCO).

■ ASSOCIATED CONTENT

Supporting Information. Current−voltage ($I-V$) characteristics of the sputtered-ITO/GZO/sputtered-ITO RRAM device, X-ray diffraction of GZO thin film with varying Ga:Zn composition, $I-V$ measurements performed by changing the directions of ground and DC bias application. This material is available free of charge via the Internet at http://pubs.acs.org.

■ AUTHOR INFORMATION

Corresponding Author
*E-mail: jmoon@yonsei.ac.kr.

■ ACKNOWLEDGMENT

This research was supported by the Basic Science Research Program through the National Research Foundation of Korea (NRF) funded by the Ministry of Education, Science and Technology (2009-0086302). It was also partially supported by the Second Stage of the Brain Korea 21 Project.

■ REFERENCES

(1) Shen, G.; Xu, J.; Wang, X.; Huang, H.; Chen, D. *Adv. Mater.* **2011**, *23*, 771–775.
(2) Kawazoe, H.; Yasukawa, M.; Hyodo, H.; Kurita, M.; Yanagi, H.; Hosono, H. *Nature* **1997**, *389*, 939–942.
(3) Wagner, J. F. *Science* **2003**, *300*, 1245–1246.
(4) Sze, S. M.; Keszler, D. A.; Presley, R. E. *Transparent Electronics*; Springer: New York, 2008; p4.
(5) Frenzel, H.; Lajn, A.; Wenckstern, H.; Lorenz, M.; Schein, F.; Zhang, Z.; Grundmann, M. *Adv. Mater.* **2010**, *22*, 5332–5349.
(6) Yoon, S.-M.; Jung, S.-W.; Yang, S.-H.; Byun, C.-W.; Hwang, C.-S.; Ishiwara, H. *J. Electrochem. Soc.* **2010**, *157* (7), H727–H733.
(7) Faber, H.; Burkhardt, M.; Jedaa, A.; Kälblein, D.; Klauk, H.; Halik, M. *Adv. Mater.* **2009**, *21*, 3099–3104.
(8) Kwon, D.-H.; Kim, K. M.; Jang, J. H.; Jeon, J. M.; Lee, M. H.; Kim, G. H.; Li, X.-S.; Park, G.-S.; Lee, B.; Han, S.; Kim, M.; Hwang, C. S. *Nat. Nanotechnol.* **2010**, *5*, 148–153.
(9) Park, J.; Biju, K. P.; Jung, S.; Lee, W.; Lee, J.; Kim, S.; Park, S.; Shin, J.; Hwang, H. *IEEE Electron Device Lett.* **2011**, *32*, 476–478.
(10) Son, J. Y.; Shin, Y.-H.; Kim, H.; Jang, H. M. *ACS Nano* **2010**, *4*, 2655–2658.
(11) Cao, X.; Li, X.; Gao, X.; Liu, X.; Yang, C.; Yang, R.; Jin, P. *J. Phys. D: Appl. Phys.* **2011**, *44*, 255104.
(12) Kim, S.; Moon, H.; Gupta, D.; Yoo, S.; Choi, Y.-K. *IEEE Trans. Electron. Dev.* **2009**, *56*, 696–699.
(13) Chen, Y.-S.; Wu, T.-Y.; Tzeng, P. -J.; Chen, P.-S.; Lee., H.-Y.; Lin, C.-H.; Chen, F.; Tsai, M.-J. *Symp. VLSI Technol.* **2009**, 37–38.
(14) Son, J. Y.; Kim, D.-Y.; Kim, H.; Maeng, W. J.; Shin, Y.-S.; Shin, Y.-H. *Electrochem. Solid-State Lett.* **2011**, *14*, H311–H313.
(15) Zhang, L.; Zhu, M.; Huang, R.; Gao, D.; Kuang, Y.; Shi, C.; Wang, Y. *ECS Trans.* **2010**, *27*, 3–8.
(16) Chien, W. C.; Chen, Y. C.; Chang, K. P.; Lai, E. K.; Yao, Y. D.; Lin, P.; Gong, J.; Tsai, S. C.; Hsieh, S. H.; Chen, C. F.; Hsieh, K. Y.; Liu, R.; Lu, C.-Y. *IEEE International Memory Workshop 2009*; IEEE: Piscataway, NJ, 2009; Vol. 91, pp 1−2.
(17) Yang, M. K.; Park, J.-W.; Ko, T.-K.; Lee, J.-K. *Appl. Phys. Lett.* **2009**, *95*, 042105.
(18) Seo, J. W.; Park, J.-W.; Lim, K. S.; Yang, J.-H.; Kang, S. J. *Appl. Phys. Lett.* **2008**, *93*, 223505.
(19) Yang, M.; Zhang, P.-J.; Liu, Z.; Liao, Z.; Pan, X.-Y.; Liang, X.-J.; Zhao, H.-W.; Chen, D. *Chin. Phys. B* **2010**, *19*, 037304.
(20) Shi, L.; Shang, D.; Sun, J.; Shen, B. *Appl. Phys. Express* **2009**, *2*, 101602.
(21) Liu, K.-C.; Tzeng, W.-H.; Chang, K.-M.; Chan, Y.-C.; Kuo, C.-C. *Microelectron. Eng.* **2011**, *88*, 1586–1589.
(22) Chen, M.-C.; Chang, T.-C.; Huang, S.-Y.; Chen, S.-C.; Hu, C.-W.; Tsai, C.-T.; Sze, S. M. *Electrochem. Solid-State Lett.* **2010**, *13*, H191–193.
(23) Misra, P.; Das, A. K.; Kukreja, L. M. *Phys. Status Solidi C* **2010**, *7*, 1718–1720.
(24) Kao, Y.-C.; Hong, F. *Nanotechnology* **2011**, *22*, 185303.
(25) Kim, D.; Jeong, Y.; Song, K.; Park, S.-K.; Cao, G.; Moon, J. *Langmuir* **2009**, *25*, 11149–11154.
(26) Chang, W.-Y.; Lai, Y.-C.; Wu, T.-B.; Wang, S.-F.; Chen, F.; Tsai, M.-J. *Appl. Phys. Lett.* **2008**, *92*, 022110.
(27) Chen, M.-C.; Chang, T.-C.; Tsai, C.-T.; Huang, S.-Y.; Chen, S.-C.; Hu, C.-W.; Sze, S. M.; Tsai, M.-J. *Appl. Phys. Lett.* **2010**, *96*, 262110.
(28) Dearnaley, G.; Stoneham, A. M.; Morgan, D. V. *Rep. Prog. Phys.* **1970**, *33*, 1129–1191.
(29) Chudnovskii, F. A.; Odynets, L. L.; Pergament, A. L.; Stefanovich, G. B. *J. Solid State Chem.* **1996**, *122*, 95–99.
(30) Odagawa, A.; Katoh, Y.; Kanzawa, Y.; Wei, Z.; Mikawa, T.; Muraoka, S.; Takagi, T. *Appl. Phys. Lett.* **2007**, *91*, 133503.
(31) Janousch, M.; Meijer, G. I.; Staub, U.; Delley, B.; Karg, S. F.; Andreasson, B. P. *Adv. Mater.* **2007**, *19*, 2232–2235.
(32) Yang, J. J.; Miao, F.; Pickett, M. D.; Ohlberg, D. A. A.; Stewart, D. R.; Lau, C. N.; Williams, R. S. *Nanotechnology* **2009**, *20*, 215201.
(33) Courtade, L.; Turquat, C.; Muller, C.; Lisoni, J. G.; Goux, L.; Wouters, D. J. *NVMTS* **2007**, 1–4.
(34) Lv, H. B.; Yin, M.; Song, Y. L.; Fu, X. F.; Tang, L.; Zhou, P.; Zhao, C. H.; Tang, T. A.; Chen, B. A.; Lin, Y. Y. *IEEE Electron. Devices Lett.* **2008**, *29*, 47–49.
(35) Jeong, Y.; Song, K.; Jun, T.; Jeong, S.; Moon, J. *Thin Solid Films* **2011**, *519*, 6164–6168.
(36) Jeong, S.; Ha, Y.-G.; Moon, J.; Facchetti, A.; Marks, T. J. *Adv. Mater.* **2009**, *21*, 1346–1350.
(37) Jeong, H. Y.; Lee, J. Y.; Choi, S.-Y.; Kim, J. W. *Appl. Phys. Lett.* **2009**, *95*, 162108.
(38) Sugiyama, K.; Ishii, H.; Ouchi, Y. *J. Appl. Phys.* **2000**, *87*, 295–298.
(39) Biju, K. P.; Liu, X.; Bourim, E. M.; Kim, I.; Jung, S.; Siddik, M.; Lee, J.; Hwang, H. *J. Phys. D: Appl. Phys.* **2010**, *43*, 495104.
(40) Sze, S. M. *Physics of Semiconductor Devices*; Wiley: New York, 1981; p227.
(41) Mott, N. F.; Gurney, R. W. *J. Chem. Educ.* **1941**, *18*, 249.
(42) Rose, A. *Phys. Rev.* **1955**, *97*, 1538–1544.
(43) Chang, K. M.; Tzeng, W. H.; Liu, K. C.; Lai, W. R. *ECS Trans.* **2010**, *28*, 119–126.
(44) Shang, D. S.; Wang, Q.; Chen, L. D.; Dong, R.; Li, X. M.; Zhang, W. Q. *Phys. Rev. B* **2006**, *73*, 245427.
(45) Kinoshita, K.; Okutani, T.; Tanaka, H.; Hinoki, T.; Agura, H.; Yazawa, K.; Ohmi, K.; Kishida, S. *Solid-State Electron.* **2011**, *58*, 48–53.
(46) Kinoshtia, K.; Okutani, T.; Tanaka, H.; Hinoki, T.; Yazawa, K.; Ohmi, K.; Kishida, S. *Appl. Phys. Lett.* **2010**, *96*, 143505.
(47) Gonçalves, A. S.; Góes, M. S.; Fabregat-Santiago, F.; Moehl, T.; Davolos, M. R.; Bisquert, J.; Yanagida, S.; Nogueira, A. F.; Bueno, P. R. *Electrochim. Acta* **2011**, *56*, 6503–6509.
(48) Song, K.; Jung, Y.; Kim, Y.; Kim, A.; Hwang, J. K.; Sung, M. M.; Moon, J. *J. Mater. Chem.* **2011**, *21*, 14646–14654.